



Core-shell catalyst pellets for effective reaction heat management

Ronny Tobias Zimmermann^a, Sebastian Weber^{b,c}, Jens Bremer^d, Vesselin Idakiev^e,
Reihaneh Pashminehazar^c, Thomas Lennon Sheppard^{b,c}, Lothar Mörl^e, Kai Sundmacher^{a,f,*}

^a Otto von Guericke University, Chair for Process Systems Engineering, Universitätsplatz 2, 39106 Magdeburg, Germany

^b Karlsruhe Institute of Technology (KIT), Institute of Catalysis Research and Technology, Hermann-von-Helmholtz-Platz 1, 76344 Eggenstein-Leopoldshafen, Germany

^c Karlsruhe Institute of Technology (KIT), Institute for Chemical Technology and Polymer Chemistry, Engesserstr. 20, 76131 Karlsruhe, Germany

^d Clausthal University of Technology, Institute of Chemical and Electrochemical Process Engineering, Leibnizstraße 17, 38678 Clausthal-Zellerfeld, Germany

^e Otto von Guericke University, Institute of Apparatus and Environmental Technology, Universitätsplatz 2, 39106 Magdeburg, Germany

^f Max Planck Institute for Dynamics of Complex Technical Systems, Department for Process Systems Engineering, Sandtorstr. 1, 39106 Magdeburg, Germany

ARTICLE INFO

Keywords:

Core-shell catalyst pellets
X-ray computed tomography
Fluidized-bed coating
Carbon dioxide methanation
Mass transport limitation

ABSTRACT

Catalyst research is concerned with synthesizing increasingly active materials, leading to safety issues at reactor scale, unless the reaction heat release is controllable. Computational studies predict that core-shell pellets with catalytically active core and inert shell are beneficial for this purpose, compared to established concepts such as catalyst pellet dilution. At high temperatures, reactant diffusion through the shell becomes rate-determining, resulting in a well-controllable heat release rate, which prevents further temperature increase. Here, industrial catalyst pellets were coated in a fluidized-bed pilot plant, demonstrating large-scale production feasibility. The obtained pellets were characterized via Dynamic Image Analysis, Scanning Electron Microscopy and X-ray Computed Tomography. Conducted CO₂ methanation experiments confirm the predicted trends, if the applied shell is fully closed. Furthermore, mathematical and experimental studies demonstrate, that the inert shell shifts selectivity. Based on this work, safer and yet economical reactor operation is anticipated also for other reaction systems.

1. Introduction

Power-to-X technologies are an opportunity to store electrical energy in the form of chemical compounds [1]. For this purpose, excess renewable energy is used for hydrogen generation via electrochemical water-splitting. Subsequently, hydrogen is converted to chemicals with existing infrastructure, such as methane (Substitute Natural Gas), ammonia, or methanol. In particular, the synthesis of carbon-based products also offers the possibility for reducing carbon dioxide emissions, by consuming it as a reactant. However, the volatile supply of surplus renewable energy makes these processes technologically challenging, due to unsteady process conditions [2,3].

For example, the synthesis of methane, methanol, and ammonia is often conducted heterogeneously catalyzed in wall-cooled multi-tubular fixed-bed reactors. These reactors are designed for intensive reaction heat removal, to keep the reactor temperature within desired bounds. Nevertheless, changes in process conditions can lead to uncontrollable reactor behavior, known as thermal runaway. In this case, the reaction heat release leads to an increase of reactor temperature and in

consequence, to a further increase of heat release, as the reaction becomes faster. This causes a feedback loop, as reaction rate rises approximately according to the Arrhenius-law (even in presence of internal mass transport limitation), while the heat removal rate increases linearly with coolant temperature. The resulting reactor temperature rise may cause selectivity decrease, catalyst deactivation or even material damage [4,5]. Evidently, effective heat management is crucial for safe reactor operation and has been researched for decades with focus on stationary reactor operation [6]. Nevertheless, if load-flexible reactor operation is expected, controllable conditions have to be maintained at all possible steady states, and also during all dynamic transitions in between. Hence, recent works also consider safe reactor design under dynamic conditions [7–9]. Kreitz et al. [10], for example, studied the dynamic operation of micro-structured reactors. Even though such reactors exhibit a large heat transfer areas, temperature peaks of about 150 K were observed for low-frequency changes of the inlet conditions. Such studies help to identify infeasible operation conditions in advance. However, the number of possible dynamic scenarios, which can be considered is limited (e.g., due to computational power or experimental effort), and in practical applications unforeseen situations might arise, e.

* Corresponding author.

E-mail address: sundmacher@mpi-magdeburg.mpg.de (K. Sundmacher).

<https://doi.org/10.1016/j.cej.2022.140921>

Received 13 September 2022; Received in revised form 7 December 2022; Accepted 9 December 2022

Available online 19 December 2022

1385-8947/© 2022 The Author(s). Published by Elsevier B.V. This is an open access article under the CC BY license (<http://creativecommons.org/licenses/by/4.0/>).

Nomenclature			
<i>Latin</i>		S	selectivity/ -
A	area/ m^2	T	temperature/ K
d	diameter/ m	V	volume/ m^3
D	diffusion coefficient/ $m^2 s^{-1}$	x	mole fraction/ -
F	flow/ $m^3 s^{-1}$	X	conversion/ -
K	equilibrium constant/ -	<i>Greek</i>	
L	length/ m	δ	Shell thickness/ m
M	molar mass/ $kg mol^{-1}$	ε	porosity/ -
N	flux/ $mol m^{-2} s^{-1}$	η	effectiveness factor/ -
p	pressure/ Pa	ν	stoichiometric coefficient/ -
r	reaction rate/ $mol m^{-3} s^{-1}$	ξ	extent of reaction/ -
R	ideal gas constant/ $J mol^{-1} K^{-1}$	Φ	Thiele modulus/ -

g., due to aging of the catalyst or fouling in the coolant system. Thus, it is indispensable to design reactors, where runaway conditions can be generally avoided.

An effective opportunity is heat release control by external mass transport limitation of the reactants to the catalyst pellets, as shown in computer-based studies by Zimmermann et al. [11,12]. This can be done, e.g., by applying an inert shell onto the active catalyst pellets, resulting in so-called core-shell catalyst pellets. The inert shell is tailored, such that the mass transport through the inert shell becomes rate-determining particularly at critical reactor temperatures. In this case, the effective reaction rate and thus the heat release rate is approximately independent of temperature, as shown in Fig. 1. Hence, a further increase of reactor temperature is prevented by the linearly increasing heat removal rate, minimizing the risk of uncontrollable conditions. Besides influencing the effective reaction rate of the catalyst pellets, the inert shell may also affect selectivity of the catalyst pellets. This can occur in principle due to different mass transport rates of reactants and products through the shell, influencing the chemical equilibrium.

These potential benefits have to be distinguished from the properties of core-shell pellets prepared with zeolitic materials (a.k.a. 'membrane-encapsulated catalysts'), which arise from the component-specific permeability of zeolites, such as protection against catalyst poisons,

increased sintering resistance and shape-selectivity [13]. However, if these component-specific permeabilities are not required less expensive materials can be used. In this case, the selectivity of the catalyst pellets does not depend on the material properties at all, if the diffusion rate through the inert shell is rate-determining, but rather on the properties of the reacting components. Furthermore, zeolitic core-shell materials are often manufactured at sub-millimeter scale, which is too small for application in industrial fixed-bed reactors, due to the high pressure loss involved. However, so-called 'egg-shell' catalyst pellets are frequently used in industrial application. These consist of an inert, sometimes even non-porous core surrounded by a catalytically active shell. A typical application is the oxidation of o-xylene to phthalic anhydride [14]. By employing the 'egg-shell' concept, internal mass transport resistances in the catalyst pellets are reduced and thus the often cost-intensive active material is used more effectively in the reactor.

Capece & Dave [15] presented an approach to prepare coated catalyst pellets at lab-scale by fluidized-bed coating. In this process, pellets are fluidized in a gas stream, while a suspension is sprayed onto them in a fluidization chamber. While the liquid suspension evaporates, a solid layer forms around the substrate pellets. The procedure is subject to a complex interplay of material properties of the substrate pellets, the suspension, as well as different process conditions (e.g., spray rate, gas temperature, and velocity) and requires extensive experimental know-how. Werner et al. [16] summarize several fundamental phenomena. After coating, a calcination step is required for removing binding agents, which adds an additional challenge. The applied coating might crumble off, delaminate, or even tear the pellets apart [17]. Nevertheless, a successful procedure allows for coating pellets of various shapes and sizes with controllable coating thickness according to the demands of the catalytic process. In addition, fluidized bed-coating is established at industrial scale and has proven to be suitable to prepare the aforementioned 'egg-shell' catalyst pellets [18].

The aim of this work is twofold. First, the interplay of mass transport through the inert shell and chemical equilibrium of a multi-component multi-reaction system is investigated based on first physical principles. Based on this analysis, the prediction of the influence of an inert shell on the activity and selectivity of the catalyst pellets is possible. Due to its high exothermicity and use as a CO₂ neutral (or even negative) fuel source, CO₂ methanation is employed as case study. Second, industrial Ni/Al₂O₃ methanation catalyst pellets are coated with an inert shell at kilogram-scale in a fluidized-bed coating apparatus. The obtained catalyst pellets are characterized via Dynamic Image Analysis, Scanning Electron Microscopy (SEM) and X-ray Computed Tomography (XCT), in order to determine the structure and integrity of the shell. In the case of hard X-ray tomography, such analysis is non-invasive and can cover large fields of view, therefore providing a representative interpretation of catalyst structure. Finally, the catalytic activity and selectivity of the catalyst pellets are investigated with respect to their dependence on

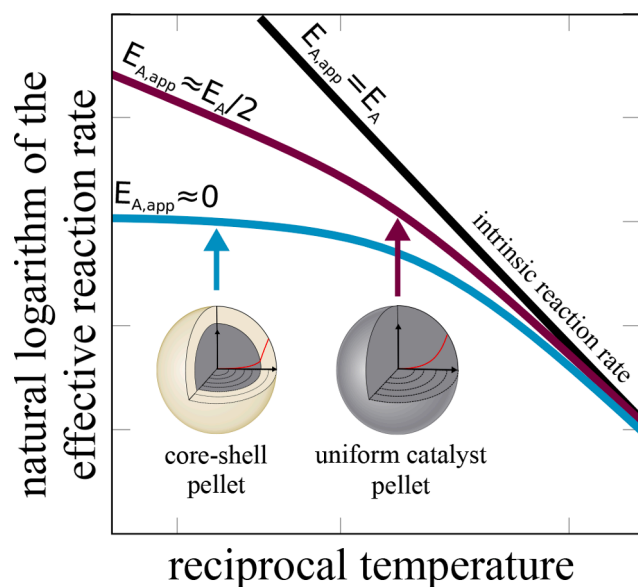


Fig. 1. Schematic comparison of uniform catalyst pellets and core-shell catalyst pellets in an Arrhenius Plot.

temperature and compared to pellets without inert shell and to crushed catalyst pellets.

2. Experimental

2.1. Core-Shell Catalyst Pellet Preparation

To validate the model based results, spherical Ni/Al₂O₃ catalyst pellets (SPP2080-IMRC, [19]) are coated with an inert shell, as schematically shown in Fig. 2. For this purpose an aluminum oxide suspension is prepared. At first, polyvinyl alcohol (PVA, Mowiol(R) 8–88, Kuraray Europe GmbH) is stirred into distilled water at 343 K. After complete dissolution of PVA, pseudo-boehmite powder (Disperal P2W (R), Sasol Germany GmbH) is added and vigorously stirred for 30 min. Subsequently α -alumina powder (1.65 μ m, BA-2, xtra GmbH) is added and stirred for another 90 min. In total, the mass fractions in the suspension are 5 % pseudo-boehmite powder, 10 % α -alumina powder, 1.5 % polyvinyl alcohol and 83.5 % distilled water.

As the catalyst pellets' availability is limited, 0.15 kg thereof is diluted with 1.35 kg inert γ -alumina pellets (2.5 mm, Sasol Germany GmbH) and put into the fluidization chamber of a fluidized bed coating pilot plant. The suspension is dosed into the fluidization chamber of a pilot plant by a bottom-spray two-fluid nozzle (Mod. 940, Düsen-Schlick GmbH, Germany). A peristaltic pump conveys the solution from a tank to the nozzle. The cylindrical fluidization chamber (inner diameter 200 mm) is made of temperature-resistant borosilicate glass. Additionally, ambient air is sucked in by a pressure blower and heated up, before entering the fluidized bed chamber through a perforated disk. After passing the fluidized bed, the air enters a calming zone and overspray particles are separated via a cyclone and a filter. Every 10 min samples are taken and the coated catalyst pellets are separated from the inert pellets into ceramic dishes for calcination in a furnace. The furnace is heated from ambient conditions to 823 K with a heating rate of 1 K/min, to remove the organic binder and to calcine the applied pseudo-boehmite. The temperature was held for 3.5 h and subsequently the pellets were cooled down to ambient temperature in the closed furnace. Samples taken after 0 min (calcined catalyst pellets without coating), 10 min, 30 min, and 50 min process time were then investigated in detail.

2.2. Dynamic Image Analysis

A pellet imaging system CAMSIZER®(Retsch Technology) was used to quantify the size of the coated pellets. With this equipment several parameters can be measured for an arbitrary pellet collective of d_p from 20 μ m to 30 mm at the same time. The principle of dynamic image analysis according to ISO-13322-1 and -2 is applied. The sample is placed on a vibrating chute via the feed hopper. In the chute they are separated and subsequently fall through a camera field to be measured (two cameras are available, basic and zoom camera). The cameras binarize the captured shadow and calculate several parameters. Depending on the pellet shape, a different pellet diameter can be used as the basis for displaying the pellet size distribution. In this work, the d_{area} -mode was chosen (50 measurements per second with both

cameras), according to which the respective apparent catalyst pellet volume is calculated.

2.3. Scanning Electron Microscopy

Samples for cross-sections are embedded in transparent epoxy resin, ground manually under watercooling (grit 180 to grit 2500), polished semiautomatically using polycrystalline diamond suspension (3 μ m) and water-based lubricant for 8 min at 15 N and finished semiautomatically using alumina suspension (0.06 μ m) for 3 min at 15 N. During preparation, the height of the samples is measured using a Nikon Digimicro MS-11C to ensure a central surface for SEM investigations. After preparation, samples are sputter-coated with gold to prevent charge build-up.

SEM analyses are performed using a FEI Scios DualBeam (Thermo-Fisher Scientific, Waltham, MA, USA) microscope equipped with a TEAM Trident system (EDAX, AMETEK GmbH, Weiterstadt, Germany). Secondary electron (SE) and backscattered electron (BSE) contrast are used to image topography and microstructure. EDS is performed for integral and local analyses of the chemical composition.

2.4. X-ray Tomography

X-ray computed tomography (XCT) measurements were carried out using a Zeiss Xradia Versa 520 X-ray microscope (Pleasanton, United States). Selected whole catalyst pellets were scanned with a 4X objective lens in binning 2 mode using a tungsten X-ray source. Measurements were performed at 40 kV and 76 μ A using a low energy filter to optimize transmission and signal to noise ratio. The chosen setting provided an optical magnification of 3.95 and voxel size of 2.85 μ m. 2041 projections were acquired over an angular range of 0 to 360 ° with an exposure time of each 1000 ms. The total measurement time per sample was about 2 h. Tomographic reconstructions were performed with the commercial software package Zeiss XMReconstructor, using a filtered back-projection type algorithm. The tomograms were corrected for beam hardening. Image analysis of the tomography data was performed with Avizo v.9.7.0 (Thermo Fisher Scientific) as discussed in detail in SI D.2.

2.5. Catalytic Activity Measurements

To perform catalytic activity measurements, three catalyst pellet spheres are placed into a quartz glass tube ($d_{tube} = 8$ mm), with each sphere separated by a quartz glass bead (2.5 mm diameter). The spheres are fixed with quartz glass wool from each side and 0.5 g silicon carbide is placed upstream of the catalyst spheres, to ensure isothermal and uniformly distributed gas flow. The silicon carbide is also kept in place by quartz glass wool. Type K thermocouples are placed before and behind the packing. The latter is considered as reaction temperature. The setup is also used with powder of the calcined SPP2080-IMRC catalyst (415 – 500 μ m sieve fraction) of crushed catalyst spheres, which is diluted with a 1:9 ratio in silicon carbide powder.

After the glass tube is placed into a furnace and sealed, gases (CO₂ 3.0, H₂ 5.0, He 5.0, Westfalen AG) are supplied via mass flow controllers

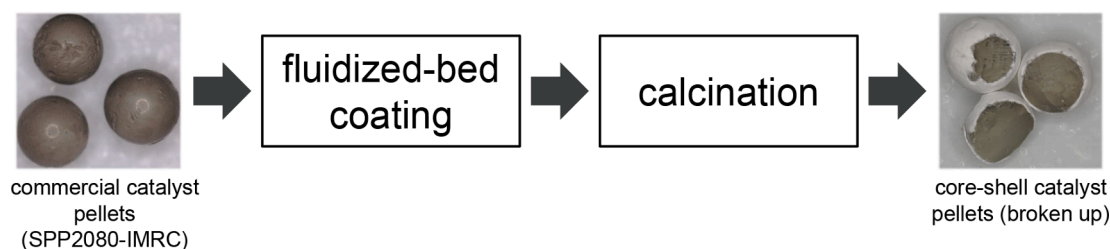


Fig. 2. Preparation scheme of core-shell catalyst pellets from spherical Ni/Al₂O₃ catalyst pellets (SPP2080-IMRC, [19]). The core-shell catalyst pellets were broken up, to reveal their layered structure.

(El-Flow®Select, Bronkhorst Deutschland Nord GmbH). The product gas is cooled down to 276 K to condense water and a constant flow of 15 Nml/min nitrogen (N₂ 5.0, Westfalen AG) is added as internal standard. Potentially remaining water is separated with a membrane, before analyzing the product gases using gas chromatography (490 Micro GC System, Agilent Technologies, Inc.).

Before catalytic activity measurements, the catalyst is dried at a furnace temperature of 393 K with 120 Nml/min of a 1:1 mixture of H₂ and He. Afterward, the furnace temperature is increased to 673 K and the catalyst is reduced for eight hours at the same gas composition. Subsequently, the catalyst is aged at reaction conditions (F_{CO₂} = 20 Nml/min, F_{H₂} = 80 Nml/min, F_{H₂O} = 100 Nml/min, p = 1.2 bara) at 773 K for eight hours. Five product gas samples are taken at each furnace temperature, following a step change profile from 773 to 523 K in steps of 25 K. The temperature difference before and behind the packing was below 7 K and the furnace temperature is up to 15 K higher than the reaction temperature. The carbon balance was closed to more than 99 % in all cases.

3. Results & Discussion

In the first section of the results, the reaction rates of catalyst pellets are derived in the presence of mass transport limitation through an inert shell. Based on this, the effect of an inert shell on the selectivity of core-shell pellets is discussed using the CO₂ methanation system as example. In the second section, the fluidized-bed coating results of industrial Ni/Al₂O₃ methanation catalyst pellets with an alumina shell are demonstrated. A detailed characterization of the obtained alumina shell based on XCT analyses is presented in the third section. The fourth section deals with the analysis of catalytic activity measurements, which are related to the model-based predictions from the first section and the texture data from section two and three.

3.1. Catalyst Pellet Activity and Selectivity under Mass Transport Limitation by the Inert Shell

The activity and the selectivity of a catalyst pellet is determined by calculating the fluxes across the outer pellet surface. In the following, this is done for a core-shell catalyst pellet at the limit of very fast reaction rates in the pellet cores in a simplified manner with negligible temperature gradients at steady-state. The presence of a very fast reaction rate in the context of this work is discussed in SI A. The procedure can be extended to more complex cases (e.g., non-negligible temperature gradients in the catalyst pellet, complex pellet geometries, non-negligible mass transport through the gas boundary layer) if necessary.

If the shell is very thin, its curvature can be neglected and slab geometry may be assumed. Following Fick's first law for an ideal gas, the flux of a component $i \in \{1, \dots, C\}$ through a shell of thickness δ is

$$N_i = -\frac{D_i}{RT} \frac{dp_i}{dr} \approx \frac{D_i}{RT} \frac{p_{i,\text{core}} - p_{i,\text{bulk}}}{\delta}. \quad (1)$$

Hence, to calculate the fluxes of all components through the inert shell, the partial pressures at the interface between catalyst pellet core and shell have to be determined. In the presence of fast reaction rates, the chemical composition at the core-shell interface approaches the equilibrium composition ($p_{i,\text{core}} \approx p_{i,\text{eq}}$). Consequently, the equilibrium condition holds for each linearly independent reaction $j \in \{1, \dots, R\}$.

$$K_j = \prod_{i=1}^C p_{i,\text{eq}}^{\nu_{ij}} \quad (2)$$

The number of components is typically larger than the number of linearly independent reactions, and thus the equation system has to be supplemented by $C - R$ equations. These are the stoichiometric relations, which express the mass conservation of chemical reactions [20–22]. Accordingly, the C fluxes given by Eq. 1 are related to R potentials ξ_j ,

called the extent of reaction.

$$N_i = \sum_{j=1}^R \nu_{ij} \frac{d\xi_j}{dr} \quad (3)$$

Inserting Eq. 1 and assuming the diffusion coefficient independent of the composition (e.g., in the Knudsen diffusion regime), these can be integrated from bulk conditions to equilibrium conditions. With $\xi_{j,\text{bulk}} = 0$, the result reads

$$D_i \frac{(p_{i,\text{eq}} - p_{i,\text{bulk}})}{RT} = \sum_{j=1}^R \nu_{ij} \xi_{j,\text{eq}}. \quad (4)$$

Evidently, the extent of reaction ξ_j is defined in a similar manner as the product yield at reactor scale, but modified by the components' diffusion coefficient. Furthermore, the extent of reaction offers a convenient opportunity to calculate the pellet reaction rates with Gauß' theorem

$$r_{\text{eff},j} = \frac{\int_{V_{\text{pellet}}} r_j dV}{V_{\text{pellet}}} = \frac{\int_{A_{\text{pellet}}} \frac{d\xi_j}{dr} dA}{V_{\text{pellet}}} \approx \frac{A_{\text{pellet}}}{V_{\text{pellet}}} \frac{\xi_j}{\delta}, \quad (5)$$

from which all other catalyst performance measures, such as activity and selectivity, can be derived.

Solving the equation system analytically is only possible for simple systems, as demonstrated in SI B. In general, numerical solution techniques are required, due to the non-linear nature of the equilibrium conditions (Eq. 2). For this reason, it is illustrative to consider a specific example such as carbon dioxide methanation (CO₂M) with the reverse water gas shift reaction (RWGS) as side reaction, as shown in Fig. 3. Carbon monoxide methanation (COM) is a linear combination of CO₂M and RWGS. Thus, two equilibrium conditions determine the system.

$$K_{\text{CO}_2\text{M}}(T) = \frac{p_{\text{CH}_4,\text{eq}} p_{\text{H}_2\text{O},\text{eq}}^2}{p_{\text{CO}_2,\text{eq}} p_{\text{H}_2,\text{eq}}^4} \quad (6)$$

$$K_{\text{RWGS}}(T) = \frac{p_{\text{CO},\text{eq}} p_{\text{H}_2\text{O},\text{eq}}}{p_{\text{CO}_2,\text{eq}} p_{\text{H}_2,\text{eq}}} \quad (7)$$

$K_{\text{CO}_2\text{M}}$ and K_{RWGS} are calculated from the equilibrium constants of the steam methane reforming reaction and the water gas shift reaction taken from literature, as given in SI C.

The results for a 4:1 mixture of hydrogen and carbon dioxide at 1 bar are shown in Fig. 4 (a) at the limit of Knudsen diffusion, where diffusion coefficients differ simply by the square root of their molar masses. Furthermore, they are compared to the hypothetical case where all diffusion coefficients are the same (Fig. 4 (b)), as in this case, the mass transport through the inert shell does not shift the equilibrium partial pressures and the equilibrium state corresponds to that of the surrounding gas bulk.

From this comparison it is evident, that the mass transport through the inert shell influences the equilibrium state in the active core significantly. Two limiting cases, whether CO₂M or RWGS is preferred can be distinguished. At high temperatures, RWGS is preferred and a

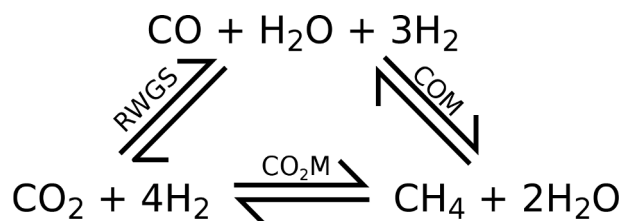


Fig. 3. Carbon dioxide methanation (CO₂M) with reverse water gas shift reaction (RWGS) as side reaction and carbon monoxide methanation (COM) as linear combination thereof.

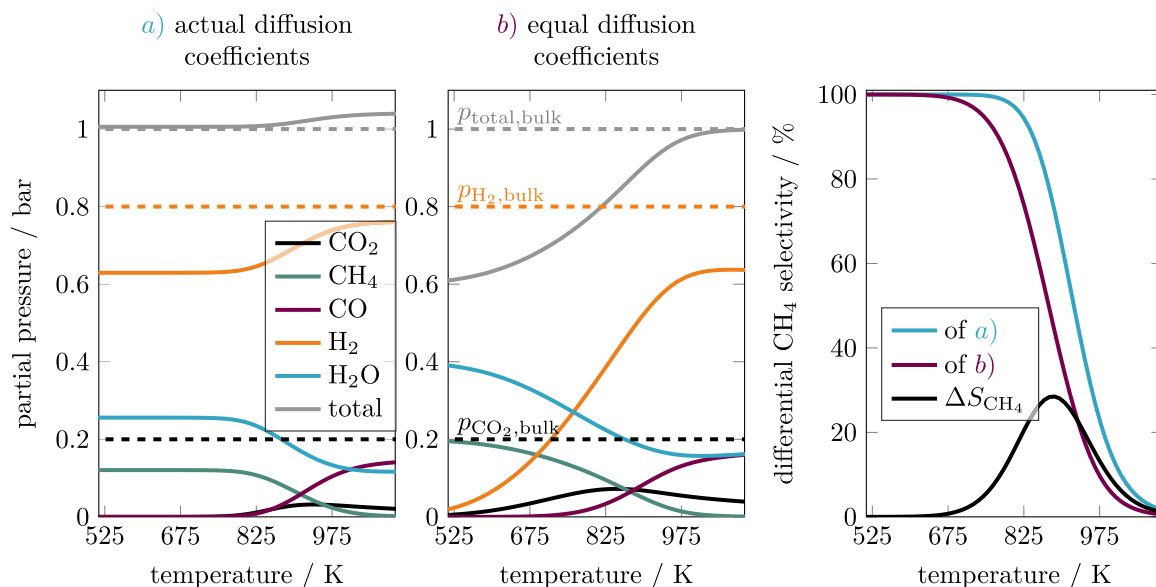


Fig. 4. Comparison of the catalyst pellet core equilibrium partial pressures of the carbon dioxide methanation system (Fig. 3) at $p_{\text{CO}_2,\text{bulk}} = 0.2$ bar, $p_{\text{H}_2,\text{bulk}} = 0.8$ bar in dependence of the temperature in the Knudsen diffusion regime: a) Calculated with actual molar masses ($\hat{=}$ actual diffusion coefficients); b) calculated with equal molar masses ($\hat{=}$ equal diffusion coefficients). Furthermore, the differential selectivity $S_{\text{CH}_4} = \xi_{\text{CO}_2\text{M}} / (\xi_{\text{CO}_2\text{M}} + \xi_{\text{RWGS}})$ is shown on the right.

significant drop in carbon dioxide partial pressure is observed, whereas the hydrogen partial pressure is almost the same as in the gas bulk. The drop of hydrogen partial pressure is only about a fifth of what is expected according to the RWGS reactions' stoichiometry, due the faster diffusion of hydrogen compared to carbon dioxide. In turn carbon monoxide and water partial pressures build up, also not according to the stoichiometry of the reaction, but according to Eq. 4 with a ratio of 1.25. Hence, the total pressure in the catalyst pellet core does not correspond to the bulk pressure. In fact, a slight overpressure is present in the catalyst pellets, which is the opposite of what might be expected for an equimolar reaction.

At low temperatures CO_2M dominates. In this case hydrogen and carbon dioxide are present in a stoichiometric ratio with respect to CO_2M in the gas bulk, with almost complete carbon dioxide consumption in the pellet core. However, hydrogen is again present in significant amounts in the catalyst pellet core, as it diffuses much quicker through the inert shell. The present hydrogen surplus is beneficial with regard to possible coke formation, which is not expected to happen in the presence of low CO_2/H_2 ratios, as discussed by Gao et al. [23]. Furthermore, methane and water partial pressures build up with a ratio of 0.47. In case of CO_2M , the ratio is closer to the reactions stoichiometry, as water and methane have similar molar masses. As in the case of RWGS, a slight overpressure is present in the pellet core, which is also in opposite of what is expected from a highly mole number reducing reaction.

In between these limits, mass transport shifts the chemical equilibrium in favor of CO_2M . The reason for this is based on three synergistic effects:

1. The overstoichiometric hydrogen partial pressure in the pellet core shifts the COM and CO_2M in favor of methane.
2. Methane is removed quicker from the pellet core than carbon monoxide, due to its higher Knudsen diffusion coefficient in the inert shell.
3. The total pressure in the catalyst pellets is elevated compared to the surrounding bulk pressure, which favors mole number reducing reactions.

Therefore, as predicted by Le Chatelier's principle, methane becomes the preferred product and carbon monoxide formation is shifted towards higher temperatures (approx. +80 K) than in the hypothetical case of

equal molar masses. This is beneficial for CO_2M , where 750 K is often the upper feasible reactor temperature. The procedure presented in this section can be readily applied to other reaction systems to determine the influence of the inert shell on the catalyst pellet behavior.

3.2. Coating Results

The applied fluidized-bed coating procedure results in very little overspray and uniform pellet growth, as shown in Fig. 5. Starting from the pellets without coating, the Sauter mean pellet diameter d_{32} increased by 0.28 mm after 50 min. The subsequent calcination step led to no determinable shrinkage of the coated catalyst pellets and they remained mechanically stable.

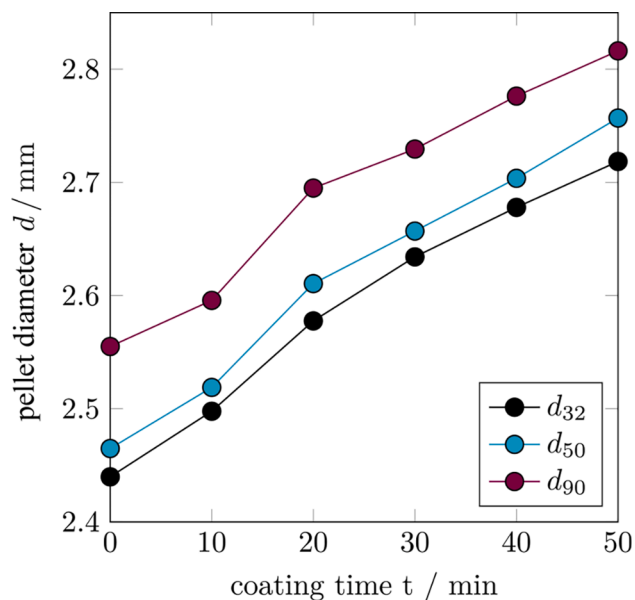


Fig. 5. Diameter of catalyst pellets over coating time as obtained by Dynamic Image Analysis. The diameter d_{32} represents the Sauter mean diameter (diameter of a sphere that has the same volume/surface area ratio), d_{50} the median diameter, and d_{90} is the diameter that 90 % of all pellets have.

As shown in Fig. 6, a clear distinction between the core of the catalyst pellets and the coating is noticeable. As analyzed in ptychographic X-ray computed tomography measurements in SI D and by Weber et al. [19], the catalyst pellet core exhibits a distinct sponge-like structure, with approximately spherical macropores embedded in a mesoporous matrix. NiO is distributed as nanoparticles, and is therefore not visible at the given magnification. In the shell of the catalyst pellets, more dense particles could be observed in a less dense matrix, which might be explained by presence of α -alumina embed in pseudo-boehmite. However, clear assignment of the phases via SEM is hardly possible. Furthermore, noticeable voids are present in the shell, which are not an issue, as long as they do not directly connect the gas bulk with the pellet surface. If the latter would be the case, bypassing of the bulk gas through the shell would become possible, and the above described effects might not be present. For this reason, a more detailed analysis of the catalyst pellets is done via XCT.

3.3. X-ray Computed Tomography

The XCT volume renderings of the four scanned catalyst pellets (after 0, 10, 30, and 50 min coating duration) are shown in Fig. 7 (a,d,g,j), respectively, with isotropic voxel sizes of 2.85 μm . The obtained XCT were segmented into different labels for further quantitative image analysis. The retrieved labels in Fig. 7 (a,d,g,j) represent the core of the catalyst pellet (gray) with the core-pores (green) as well as the shell (blue) with the shell-pores (orange).

The resolution of the XCT is not sufficient for a full analysis of the porosity as shown previously in [19]. However, in the present case it can provide a qualitative measure on the differences between the core and shell and their respective contribution to the overall resolved porosity. As the voxel size and measurement parameters are identical for each tomogram, this comparison is possible and observed differences can be carefully discussed. Furthermore, larger voids in the shell as indicated by the SEM images (Fig. 6) can be identified. The porosity distributions of the XCT depending on the d_{eq} (equivalent spherical pore diameter) of the detected pores are shown in Fig. 7 (b,e,h,k) for each coating time and

the obtained porosity and mean d_{eq} values for the XCT are summarized in Table 1.

In particular, the contribution of the shell porosity to the overall resolved porosity ϵ_{tot} is increasing with longer coating time, while the observed $d_{\text{eq,shell}}$ of the pores in the shell are not changing significantly. In the distribution of the ϵ weighted d_{eq} depending on the distance to the catalyst pellet center (d_{center}) the two different pore labels (core-pores and shell-pores) can be readily identified. The measured d_{eq} for the shell-pores are showing generally larger pores in the shell compared to the core. The resolvable d_{eq} distribution of the core is quite homogeneous and similar for all four samples. However, the resolution of the chosen XCT method is not sufficient for a complete analysis of the catalyst pore structure, which ranges from few nm up to several μm and thus requires a combination of different imaging techniques as shown in [19] (see also SI D). It is rather sufficient to identify larger outliers of the macroporosity being present in the catalysts.

In addition to a qualitative comparison of measurable porosity and pore diameters, XCT was used to analyze the thickness of the coated shell, and particularly to assess the presence of a closed shell. As shown in Fig. 6, it is also possible to determine the thickness of the shell from SEM images, however this only provides very local information limited to 2D. XCT allows for a 3D analysis of the shell as shown in Fig. 8 for three different coating times (10, 30, and 50 min).

The cuts through the XCT volumes in Fig. 8 (a-c) illustrate the increasing shell thickness with increasing coating duration. To investigate the thickness of the shell in more detail, two surfaces were computed, one for the filled catalyst core and one for exterior of the filled shell. Cuts through the rendering of the surfaces are shown in Fig. 8 (d-f). It can be observed that after 10 min coating time a closed shell was not obtained, while for 30 min coating time the thickness increased and only few voids in the shell still remained. After 50 min coating duration, a completely closed shell with increased shell thickness could be observed. Furthermore, the shortest distance of the exterior surface of the shell to the surface of the filled core was computed for each surface point. The resulting distributions of the shell thickness

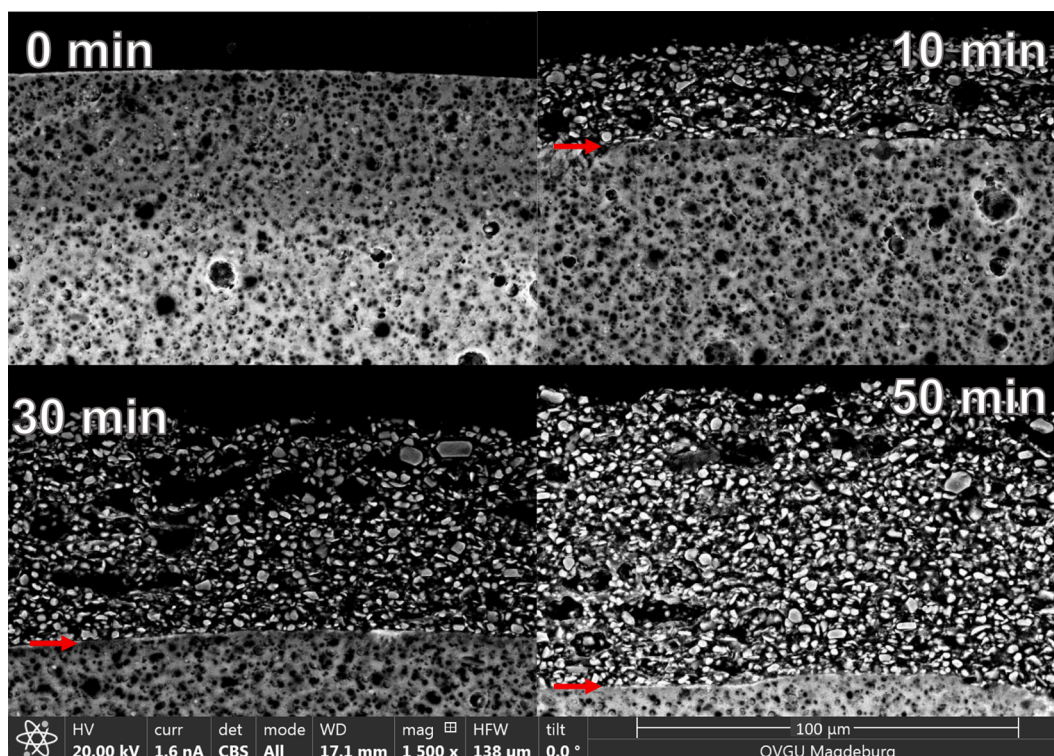


Fig. 6. SEM images of calcined samples taken after coating times of 0, 10, 30 and 50 min. Red arrows indicate the coating interfaces.

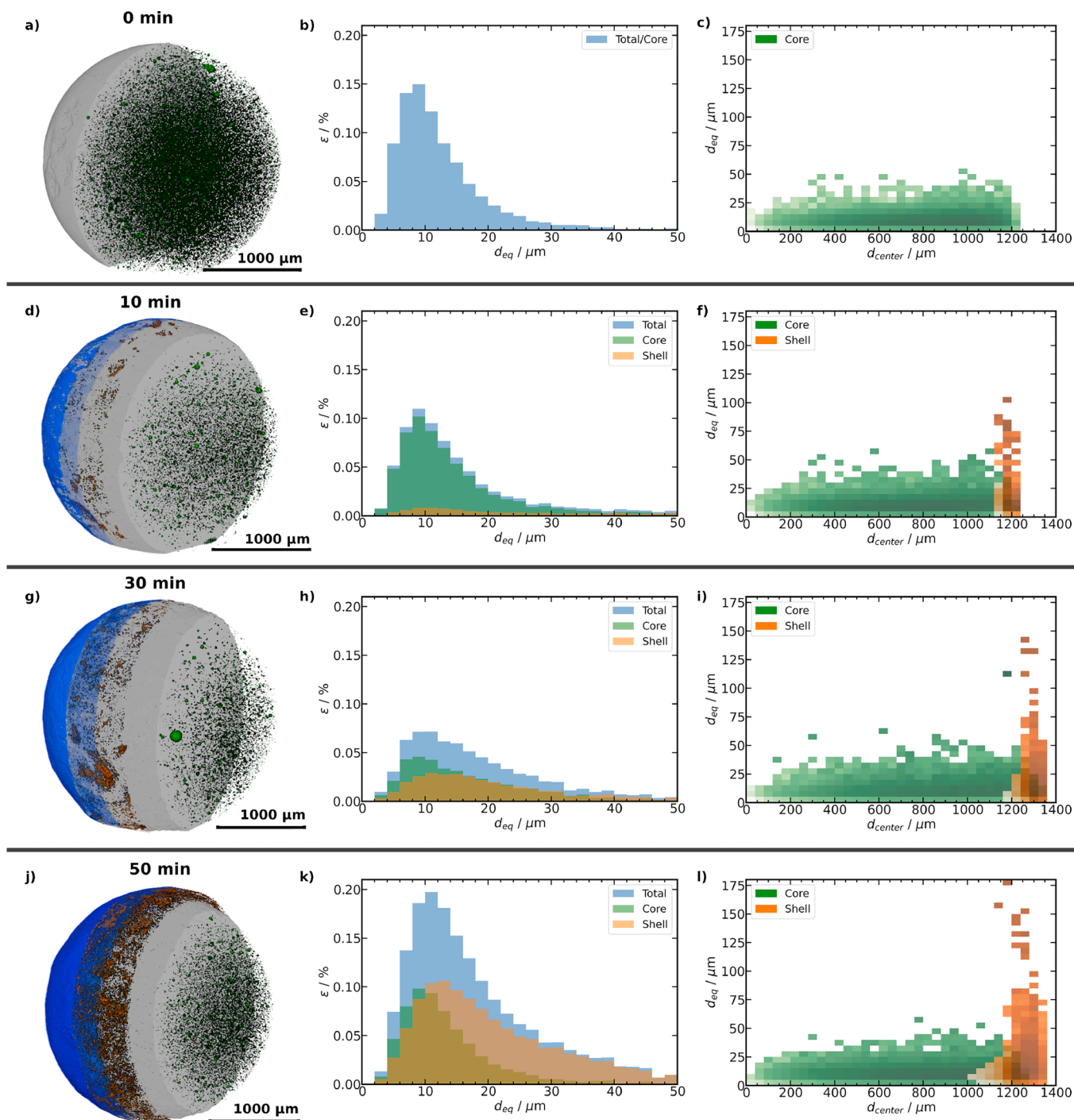


Fig. 7. XCT volume renderings of selected whole catalyst pellets with different coating times, (a) 0 min, (d) 10 min, (g) 30 min, and (j) 50 min showing each the segmented labels for the catalyst core (gray), core-pores (green), shell (blue), and shell-pores (orange). The volume renderings are cut at certain positions to highlight the different labels being present. (b,e,h,k) show the porosity depending on d_{eq} separated into total-porosity (blue), core-porosity (green) and shell-porosity (orange) for the respective samples. (c,f,i,l) show the ε weighted 2D histograms of d_{eq} depending on d_{center} distinguished into core-pores (green) and shell-pores (orange).

(δ_{shell}) are presented in Fig. 8 (g-i). The distributions clearly show the increased shell thickness with increasing coating time and allow to retrieve a mean δ_{shell} value together with its standard deviation as summarized in Table 1. The mean δ_{shell} increased from about 15 μm after 10 min, over 40 μm after 30 min and 105 μm after 50 min coating time.

In summary, the XCT results allow for a quick qualitative inspection, whether a closed shell is obtained after a certain coating duration. Furthermore, precise quantitative information about the shell thickness can be retrieved, which in combination is hardly possible with any other method. The resolution of the here applied XCT method is not sufficient

for a full porosity analysis, only voids larger than about 3 μm can be detected. A detailed study of the shell porosity is possible in future studies employing hard X-ray nanotomography, which allows sub 100 nm resolution on samples that can cover the full thickness of the shell and direct retrieval of advanced pore network models for the macropores and quantitative information about the mesoporosity are available. [24].

3.4. Catalytic Activity Experiments

To validate the computational predictions of the influence of an inert

Table 1

Quantitative information about the porosity and shell thickness retrieved from image analysis of the XCT for the studied samples.

coating time/ min	0	10	30	50
$\epsilon_{\text{tot}} / \%$	0.9	0.8	0.8	2.1
$\epsilon_{\text{core,tot}} / \%$	0.9	0.6	0.4	0.6
$\epsilon_{\text{core}} / \%$	0.9	0.7	0.4	0.8
$\epsilon_{\text{shell,tot}} / \%$	-	0.2	0.4	1.5
$\epsilon_{\text{shell}} / \%$	-	6.4	5.7	7.5
$d_{\text{eq,core}} / \mu\text{m}$	7 ± 4	8 ± 5	9 ± 5	8 ± 4
$d_{\text{eq,shell}} / \mu\text{m}$	-	11 ± 11	11 ± 9	11 ± 9
$\delta_{\text{shell}} / \mu\text{m}$	-	15 ± 12	40 ± 17	105 ± 31

shell on the pellet reaction rate and apparent selectivity, catalytic activity experiments have been performed in a lab-scale reactor, with results shown in Fig. 9. At the given conditions, detectable carbon dioxide conversion are present starting at about 523 K. The calcined catalyst powder and the calcined pellets without coating ($\cong 0$ min coating time) show slightly decreased conversion and methane selectivity, compared to their counterparts, which have not been calcined. The results of the latter are given by Weber et al. [19].

The carbon dioxide conversion of the catalyst pellets increases much slower with temperature, than the carbon dioxide conversion of the

catalyst powder, which indicates the presence of mass transport limitations. The limiting component is likely carbon dioxide, due to its much larger molar mass, compared to hydrogen, even though both reactants are present in a stoichiometric ratio with regard to CO_2M . Apart from that, also the methane selectivity is shifted. As hydrogen diffuses much quicker into the catalyst pellets than carbon dioxide, its partial pressure is close to that of the surrounding gas bulk. Consequently, the CO_2M and the COM equilibria (Fig. 3), which are present in the center of the catalyst pellets in the presence of mass transport limitations, are shifted towards the side of methane. Furthermore, as methane has a lower molar mass than carbon dioxide, it diffuses much quicker out of the catalyst pellet. Both effects combine to an increase of about 8 % in methane selectivity from 500–550 K. The coated catalyst pellets continue these trends. The carbon dioxide conversion drops and the methane selectivity rises with increasing shell thickness, which indicates that an additional mass transport limitation is induced by the inert shell. Comparing catalyst pellets without shell to the pellets with the thickest shell at 773 K, reveals an increase in methane selectivity by 30 %.

Apart from that, the mass transport limitation of the inert shell does also shift the temperature dependence of the carbon dioxide consumption rate. As shown in the Arrhenius plot (Fig. 9 (c)) the logarithm of the carbon dioxide consumption rate over the inverse temperature is a straight line for the catalyst powder, as expected in absence of transport

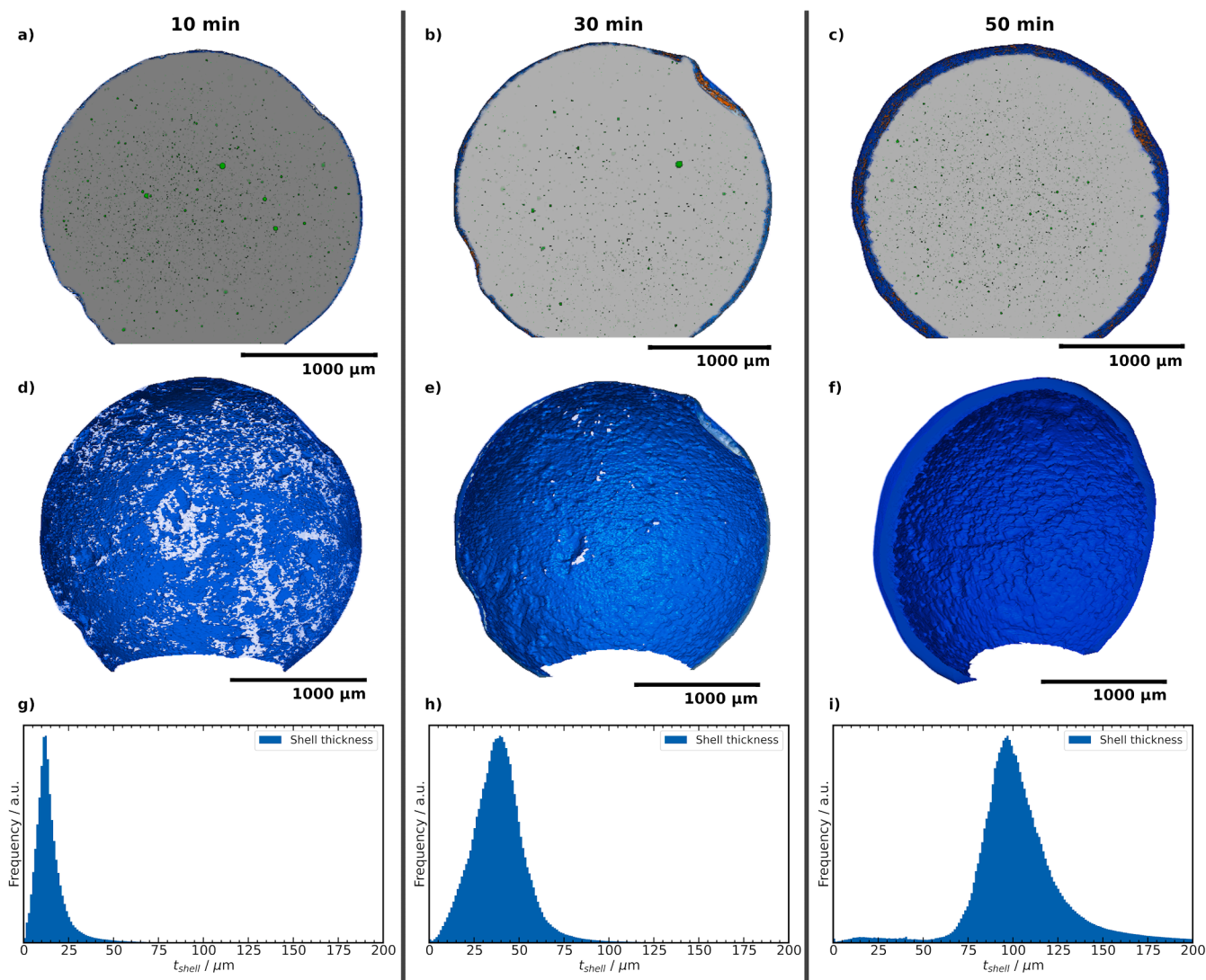


Fig. 8. Analysis of the shell thickness based on XCT depending on the coating time. (a–c) show cuts through the middle of the volume renderings with core (gray), core-pores (green), shell (blue) and shell-pores (orange) labels. (d–f) show a cut through surface renderings of the filled shell. (g–i) show the δ_{shell} distribution.

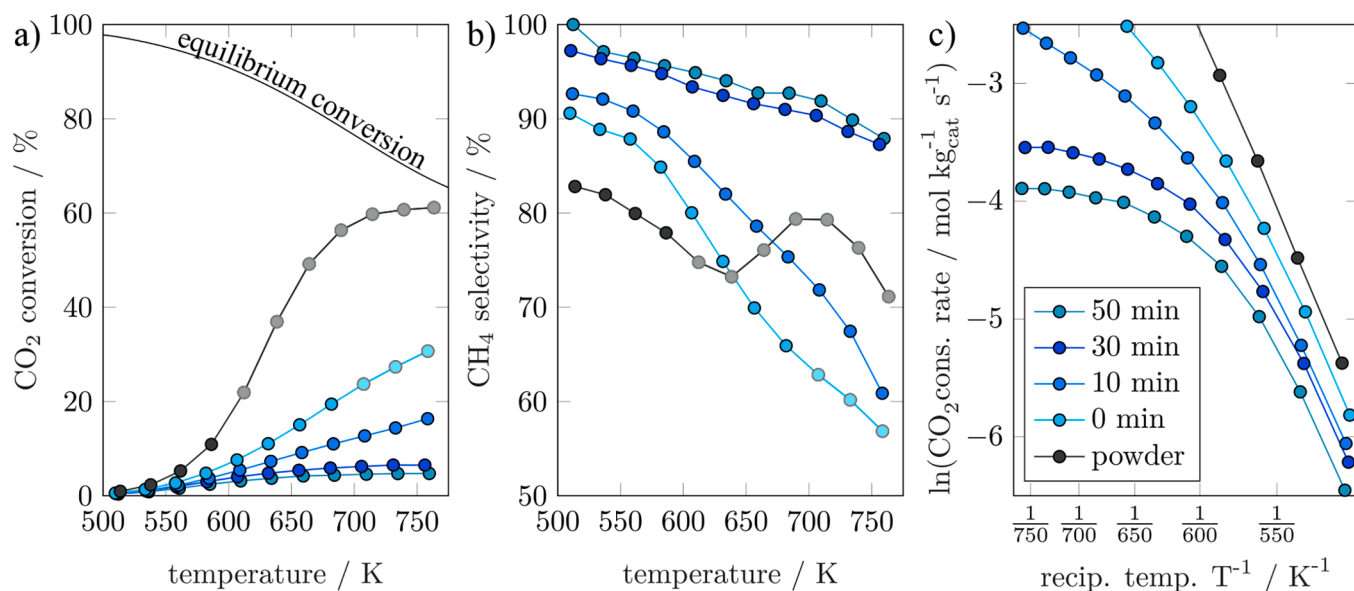


Fig. 9. Carbon dioxide conversion (a), methane selectivity (b) as well as carbon dioxide consumption rate (c) for coated and uncoated SPP2080-IMRC spheres as well as powder at $p = 1.2$ bar, $x_{\text{CO}_2} = 0.1$, $x_{\text{H}_2} = 0.4$ and $x_{\text{He}} = 0.5$. Data points with $X_{\text{CO}_2} > 20\%$ are faded, as in this case differential reaction conditions cannot be assumed. The 0 min sample and powder sample have not been introduced in the fluidized-bed, but were calcined in the same way as the fluidized-bed coating samples.

limitations. In case of the catalyst pellets without coating, the slope is equal to that of the powder at low temperatures, but starts to decrease with rising temperature, which marks the onset of mass transport limitation. At a temperature of about 700 K, the slope is about half the value of that of the powder, which indicates the presence of internal mass transport limitation.

The slope in the Arrhenius plot is further decreased for the pellet sample after 10 min coating time. However, it does not approach zero, as expected from Fig. 1. This indicates, that the pellets are operating between mass transport limitation in the active core and the inert shell. The reason for this is a very thin shell, which is not completely closed, as indicated by the XCT results in Fig. 8. In contrast, the shells of the samples after 30 and 50 min coating time are (almost) completely closed. This is also reflected in the Arrhenius plot, since for these samples the slope approaches zero at high temperatures, which indicates mass transport limitation exclusively by the inert shell.

4. Conclusion

Understanding and controlling mass transport phenomena at catalyst pellet scale yields favorable properties for industrial reactor operation. For instance, in the context of carbon dioxide methanation in fixed-bed reactors, it was shown by computer-based studies, that an inert shell on the catalyst pellets yields a well-controllable heat release rate, if the diffusion of the reactants through the inert shell is rate-determining [11,12]. This, e.g., minimizes the risk of reactor runaway and allows for reliable reactor heat control even at unsteady conditions.

To validate these results and to demonstrate the feasibility of large-scale production, commercial Ni/Al₂O₃ methanation catalyst pellets were coated with an inert alumina shell via fluidized-bed coating. After calcination, the obtained catalyst pellets were analyzed via Dynamic Images Analysis, REM and XCT. In particular, XCT revealed that a certain coating duration is required to obtain a closed shell, while the shells are generally quite homogenous.

Catalytic activity experiments confirmed the computer-based predictions. The apparent activation energy of the pellets with fully closed shell is significantly decreased at high temperatures, which indicates the expected presence of mass transport limitation through the inert shell. For catalyst pellets without (fully closed) shell, these effects were not

observed, which underlines the necessity of a defect-free shell for the mass transport through the inert shell to become rate-determining at high temperatures.

Furthermore, the coated catalyst pellets with the thickest shell exhibit a methane selectivity, which is up to 30 % higher than that of the uncoated catalyst pellets at the presence of external mass transport limitation. As concluded by a model based analysis, this effect is rooted on the interplay of the differing component mass transport rates through the inert shell, which in turn shift the equilibrium composition inside the catalyst pellets. Compared to carbon dioxide, hydrogen with the lower molar mass diffuses quicker through the inert shell into the active catalyst pellet core. Thus, hydrogen is excessively present in the pellet cores, which shifts the carbon dioxide methanation equilibrium and the carbon monoxide methanation equilibrium towards the side of methane. Additionally, the pressure is slightly elevated compared to bulk conditions and methane is removed quicker from the pellet core than the heavier side product carbon monoxide. In summary, according Le Chatelier's principle, methane becomes the favored product.

The mathematical and experimental methods used in this work can be directly applied to other reaction systems to check whether an inert shell also has a positive effect on the selectivity towards the desired product. As a rule of thumb, the formation of the product with the higher diffusion coefficient in the inert shell becomes more preferred. It is expected, that the presented core-shell catalyst pellet concept enhances reactor performance also for other challenging applications.

Declaration of Competing Interest

Ronny Zimmermann, Jens Bremer, and Kai Sundmcher have patent #WO2020/234337A1 pending as Inventors.

Data availability

Data will be made available on request.

Acknowledgments

This research work was conducted within the DFG Priority Program SPP2080 "Catalysts and reactors under dynamic conditions for energy

storage and conversion” and was funded by the Deutsche Forschungsgemeinschaft (DFG, German Research Foundation) –406914011. (Gefördert durch die Deutsche Forschungs-gemeinschaft (DFG)-406914011.) This research work was also supported by the Center of Dynamic Systems (CDS), funded by the EU-program ERDF (European Regional Development Fund).

Furthermore, this project has received funding from the European Union’s Horizon 2020 research and innovation programme under grant agreement No 731019 (EUSMI). The authors acknowledge the Paul Scherrer Institut, Villigen, Switzerland for provision of synchrotron radiation beamtime at beamline X12SA–cSAXS of the Swiss Light Source and Ana Diaz and Mirko Holler for support during beamtime. This work was partly carried out with the support of the Karlsruhe Nano Micro Facility (KNMF), a Helmholtz Research Infrastructure at Karlsruhe Institute of Technology (KIT), which provided access to FIB instruments via proposal 2020–023-028494. The authors thank Sabine Schlabach for support during FIB sample preparation.

Ronny Zimmermann is also affiliated with the International Max Planck Research School (IMPRS) for Advanced Methods in Process and Systems Engineering, Magdeburg, Germany. Generous product samples by Sasol Germany GmbH are gratefully acknowledged.

Appendix A. Supplementary data

Supplementary data associated with this article can be found, in the online version, at <https://doi.org/10.1016/j.cej.2022.140921>.

References

- [1] C. Wulf, P. Zapp, A. Schreiber, Review of Power-to-X demonstration projects in Europe, *Frontiers in Energy Research* 8 (2020) 227, <https://doi.org/10.3389/fenrg.2020.00191>.
- [2] G. Gahleitner, Hydrogen from renewable electricity: An international review of power-to-gas pilot plants for stationary applications, *International Journal of Hydrogen Energy* 38 (5) (2013) 2039–2061, <https://doi.org/10.1016/j.ijhydene.2012.12.010>.
- [3] M. Götz, J. Lefebvre, F. Mörs, A. McDaniel Koch, F. Graf, S. Bajohr, R. Reimert, T. Kolb, Renewable power-to-gas: A technological and economic review, *Renewable Energy* 85 (4) (2016) 1371–1390, <https://doi.org/10.1016/j.renene.2015.07.066>.
- [4] F. Stoessel, *Thermal Safety of Chemical Processes*, Wiley (2008), <https://doi.org/10.1002/9783527621606>.
- [5] C.-S. Kao, K.-H. Hu, Acrylic reactor runaway and explosion accident analysis, *Journal of Loss Prevention in the Process Industries* 15 (3) (2002) 213–222, [https://doi.org/10.1016/S0950-4230\(01\)00070-5](https://doi.org/10.1016/S0950-4230(01)00070-5).
- [6] A. Kummer, T. Varga, What do we know already about reactor runaway? – a review, *Process Safety and Environmental Protection* 147 (March (3)) (2021) 460–476, <https://doi.org/10.1016/j.psep.2020.09.059>.
- [7] A. Fache, F. Marias, V. Guerré, S. Palmade, Optimization of fixed-bed methanation reactors: Safe and efficient operation under transient and steady-state conditions, *Chemical Engineering Science* (2018), <https://doi.org/10.1016/j.ces.2018.08.044>.
- [8] K.L. Fischer, H. Freund, On the optimal design of load flexible fixed bed reactors: Integration of dynamics into the design problem, *Chemical Engineering Journal* 393 (2020), 124722, <https://doi.org/10.1016/j.cej.2020.124722>.
- [9] J. Bremer, K.H.G. Rätze, K. Sundmacher, CO₂ methanation: Optimal start-up control of a fixed-bed reactor for Power-to-Gas applications, *AIChE Journal* 63 (1) (2017) 23–31, <https://doi.org/10.1002/aic.15496>.
- [10] B. Kreitz, G.D. Wehinger, T. Turek, Dynamic simulation of the CO₂ methanation in a micro-structured fixed-bed reactor, *Chemical Engineering Science* (2018), <https://doi.org/10.1016/j.ces.2018.09.053>.
- [11] R.T. Zimmermann, J. Bremer, K. Sundmacher, Optimal catalyst particle design for flexible fixed-bed CO₂ methanation reactors, *Chemical Engineering Journal* 387 (2020), 123704, <https://doi.org/10.1016/j.cej.2019.123704>.
- [12] R.T. Zimmermann, J. Bremer, K. Sundmacher, Load-flexible fixed-bed reactors by multi-period design optimization, *Chemical Engineering Journal* 428 (1) (2022), 130771, <https://doi.org/10.1016/j.cej.2021.130771>.
- [13] N. Masoumifard, R. Guillet-Nicolas, F. Kleitz, Synthesis of engineered zeolitic materials: From classical zeolites to hierarchical core-shell materials, *Advanced materials (Deerfield Beach, Fla.)* 30 (16) (2018) e1704439. doi:10.1002/adma.201704439.
- [14] R. Guettel, T. Turek, Assessment of micro-structured fixed-bed reactors for highly exothermic gas-phase reactions, *Chemical Engineering Science* 65 (5) (2010) 1644–1654, <https://doi.org/10.1016/j.ces.2009.11.002>.
- [15] M. Capece, R. Dave, Application of fluidized bed film coating for membrane encapsulation of catalysts, *Powder Technology* 211 (2–3) (2011) 199–206, <https://doi.org/10.1016/j.powtec.2011.04.015>.
- [16] S.R. Werner, J.R. Jones, A.H. Paterson, R.H. Archer, D.L. Pearce, Air-suspension coating in the food industry: Part II — micro-level process approach, *Powder Technology* 171 (1) (2007) 34–45, <https://doi.org/10.1016/j.powtec.2006.08.015>.
- [17] S. Ould-Chikh, N. Brodusch, N. Crozet, M. Hemati, L. Rouleau, Understanding the key parameters for the rational design of layered oxide materials by composite sol-gel procedures, *Powder Technology* 237 (7) (2013) 255–265, <https://doi.org/10.1016/j.powtec.2012.11.010>.
- [18] R.H. Jensen, J.C. Bricker, Q. Chen, M. Tatsushima, K. Kikuchi, M. Takayama, K. Hara, I. Tsunokuma, H. Serizawa, Layered catalyst composition and processes for preparing and using the composition, *US Patent* 6,177,381 (Jan. 23 2001).
- [19] S. Weber, R.T. Zimmermann, J. Bremer, K.L. Abel, D. Poppitz, N. Prinz, J. Ilsemann, S. Wendholt, Q. Yang, R. Pashminehazar, F. Monaco, P. Cloetens, X. Huang, C. Kübel, E. Kondratenko, M. Bauer, M. Bäumer, M. Zobel, R. Gläser, K. Sundmacher, T.L. Sheppard, Digitization in catalysis research: Towards a holistic description of a Ni/Al₂O₃ reference catalyst for CO₂ methanation, *ChemCatChem* (2022), <https://doi.org/10.1002/cctc.202101878>.
- [20] R. Jackson, *Transport in porous catalysts*, Elsevier Science & Technology, 1977.
- [21] A. Burghardt, Transport phenomena and chemical reactions in porous catalysts for multicomponent and multireaction systems, *Chemical Engineering and Processing: Process Intensification* 20 (5) (1986) 229–244, [https://doi.org/10.1016/0255-2701\(86\)80016-2](https://doi.org/10.1016/0255-2701(86)80016-2).
- [22] G.R. Gavalas, *Nonlinear differential equations of chemically reacting systems*, Springer Science & Business Media, 1968.
- [23] J. Gao, Y. Wang, Y. Ping, D. Hu, G. Xu, F. Gu, F. Su, A thermodynamic analysis of methanation reactions of carbon oxides for the production of synthetic natural gas, *RSC Advances* 2 (6) (2012) 2358, <https://doi.org/10.1039/c2ra00632d>.
- [24] S. Weber, A. Diaz, M. Holler, A. Schropp, M. Lyubomirskiy, K.L. Abel, M. Kahnt, A. Jeromin, S. Kulkarni, T.F. Keller, R. Gläser, T.L. Sheppard, Evolution of hierarchically porous nickel alumina catalysts studied by X-ray ptychography, *Advanced Science* 1 (2022) 2105432, <https://doi.org/10.1002/adv.202105432>.